Highly Densified Fracture-Free Silicon-Based Electrode for High Energy Lithium-Ion Batteries

Jaekyung Sung+,[a] Namhyung Kim+,[a] Sang-Pil Kim,[b] Taeyong Lee,[a] Moonsu Yoon,[a] and Jaephil Cho*[a]

There has recently been an increasing volume of research in silicon-based anodes for high energy density lithium-ion batteries. Micron-sized composites with high tap density and a number of pores accommodating the massive volume expansion of silicon (Si) exhibit considerable electrochemical performance with high volumetric energy density. However, huge pressure on the particle during the calendering process brings about mechanical failure which causes the formation of additional by-products upon lithiation and electrical contact loss. Here, we discover specific particle size distribution based on the constructive simulation including calculation of the packing density depending on the different particle size distribution and stress evolution of each particle at high pressure. A silicon/graphite hybrid anode in which the silicon nanolayer (~15 nm) is coated on the graphite is selected to validate the simulation. This anode sustains its morphological integrity and secures its void space without crack propagation of the silicon nanolayer in the densely packed electrode. As a result, it demonstrates high initial specific capacity (>500 mAh g^{-1}), high initial Coulombic efficiency (95.2%), low electrode swelling ratio (35% at first cycle), and excellent capacity retention ratio (99.1% during 50 cycles) for high energy density lithium-ion batteries.

The urgent need to increase energy storage capability in a confined space has stimulated the painstaking research on lithium-ion batteries (LIBs) for electric vehicles with more extended driving mileage.[1–4] There are numerous ways to achieve high volumetric energy density of LIBs. The minimized use of substances that do not participate in electrochemical reactions (e.g., thin and small cell covers, separators, current collectors, conductive agents, binders, etc.) and optimized battery design parameters (e.g., N/P ratio close to ~1, high areal capacity, low electrode swelling ratio, high electrode density, and etc.) render the raised ratio of active materials (both anode and cathode) in the fixed volume of the cell.[5,6] Electrode density has been identified as one of the influential factors improving volumetric energy density. For example, the density of a pristine electrode (~1.0 g cc^{-1}) using commercial graphite anode can be increased to ~1.6 and 1.8 g cc^{-1} when the calendering process is carried out, bringing about a 30%–40% increased energy density (Figure 1a). In addition, control of the intrinsic values (e.g., gravimetric capacity, working voltage, initial Coulombic efficiency) is also a crucial factor.

The use of a silicon (Si) anode with ten times higher theoretical capacity (3579 mAh g^{-1}) than that of conventional graphite (372 mAh g^{-1}) has been attempted for a next-generation LIB system.[7–9] However, huge Si volume change, which is regarded as the main reasons for mechanical failure, unstable solid electrolyte interphase (SEI), and electrical isolation upon repeated charge-discharge process, brings about the limited cycle life and hinders the practical use.[10–12] To address these concerns, assorted strategies of nano-engineering including porous structure design and particle size control have been explored because mitigated stress of expanded Si prevents severe mechanical failure.[13–18] Nevertheless, the low tap density of these anodes causes dramatic loss of volumetric capacity. For these reasons, a number of studies regarding the micron-sized composites containing nano-sized Si have been conducted as an industrially applicable material design because of its high tap density.[19–26] When it comes to its practical application, the Si-based composites have been utilized with the graphite in the form of the blending (simple mixing graphite and Si-based composite in the electrode) and hybrid (a large amount of the graphite contained in Si-based composite) strategies.[27,28] Since the graphite is a well-established commercial anode with a low volume expansion upon lithiation (ca. 10%), slippery/deformable properties, and high electrical conductivity, it allows the Si-based composite to have low volume changes of the electrode, high electrode density from facile calendering process, and enhanced whole electrochemical performance. Notably, the hybrid strategies with more homogenous Si distribution in the material and electrode level compared to blending strategies with locally placed Si are well-known to bring about the mitigated volume expansion of the electrode (Figure 1b).[29,30]

Nevertheless, mechanical pressure upon calendering process, which further improves electrode density for high volumetric energy density, makes Si susceptible to severe

[a] J. Sung,+ N. Kim,+ T. Lee, M. Yoon, Prof. J. Cho
     Department of Energy Engineering,
     School of Energy and Chemical Engineering, Ulsan,
     National Institute of Science and Technology (UNIST)
     Ulsan 44919, South Korea
     E-mail: jpcho@unist.ac.kr
[b] Dr. S.-P. Kim
     Lab Simulation Group, Samsung SDI
     Suwon 16678, South Korea
[+] These authors contributed equally to this work.
     Supporting information for this article is available on the WWW under
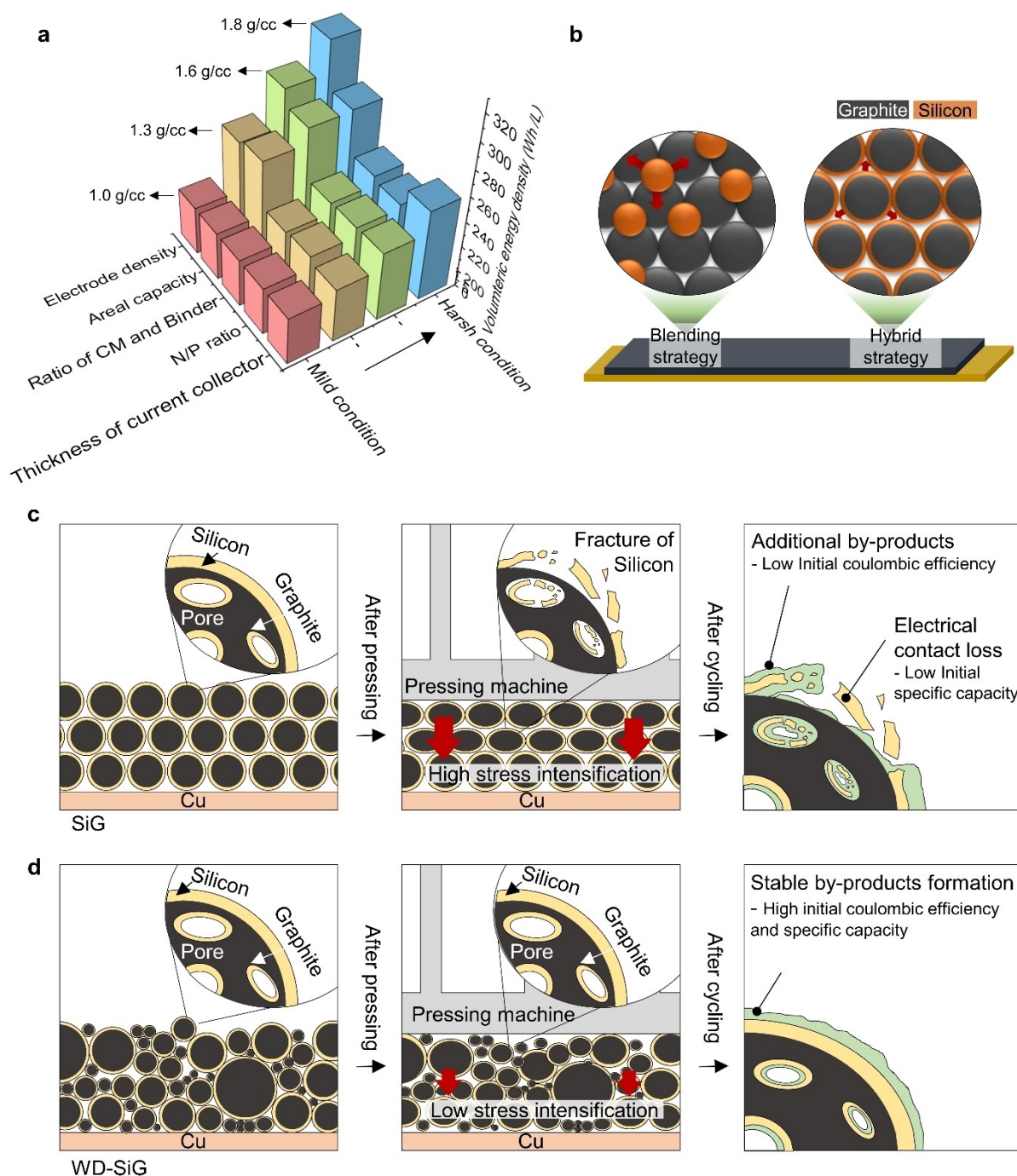   https://doi.org/10.1002/batt.202200136

Figure 1. The various factors affecting volumetric energy density. a) Three-dimensional (3D) graph, showing a correlation between volumetric energy density and the electrode/cell design factors. b) Schematic illustration of blending and composite strategies and each behavior in terms of electrode thickness changes. The red arrow indicates direction and degree of the Si volume expansion. Schematic regarding the morphological and electrochemical behavior of c) SiG and d) WD-SiG after calendering process. The pulverized Si-layer during calendering process leading to the additional by-products and electrical contact loss in SiG electrode upon cycles. The preservation of morphological integrity of Si-layer brings during calendering process brings about the stable SEI formation in WD-SiG electrode upon cycles.

fracture and pulverization unlike the slippery nature of graphite. The existence of a number of pores, which is necessary to alleviate the Si volume expansion in the composite, exacerbates these situations. It can eventually lead to the poor electrochemical performance originating from the additional by-product formation upon lithiation and electrical contact loss (Figure 1c). For these reasons, the strategies of robust surface coating with high mechanical properties (e.g., metal oxide or carbon playing a decisive role in enduring the high pressure) have been proposed for preventing breakage of Si-based anodes.[31–33] However, an excessive surface coating layer with an inactive material could not only decrease the specific capacity but also influence ionic and electrical conductivity. Therefore, there is strong motivation to realize high electrode

density without adversely impacting the electrode materials and battery performance.

The hypothesis which motivates the present study is derived from a bimodal concept that enhances the packing density of cathode materials with relatively low pressure, resulting in improved volumetric energy density.[34–36] Such a concept is expecting to be effective to avoid Si-based anode having fragile properties and the void-space being vulnerable to high pressure. To realize this concept and prove its effectiveness, we choose the Si-nanolayer embedded graphite (Si/graphite) because its particle size distribution (core technology in our strategy) of Si/graphite could be simply controlled through the selection of different sized graphite (there are diverse sized particles of graphite on the market). Through the simulation technique of discrete element method (DEM), in this work, we discovered novel particle size distribution having high packing density with low-stress intensification under high pressure generated by the process of calendering for high electrode density. Based on the simulation, a wide particle-size distribution Si/graphite hybrid (WD-SiG) was synthesized using precursors including a mixture of graphite with assorted particle size and monosilane (for Si-layer through gas decomposition process) for Si-layer. Notably, preservation of its morphological integrity without any cracking during calendering process diminishes the formation of by-products during the (dis)charging process (Figure 1d). As a result, WD-SiG has a prominent feature in retaining the electrochemical performance even with the high electrode density, which renders the unprecedented initial Coulombic efficiency (CE) of 95.2% and

capacity retention ratio of 99% for 50 cycles under densely packed electrode of 1.6 g cc^{-1}.

Results and Discussion

To ascertain optimized WD-SiG, we performed a series of blending and packing simulations based on the particle size distribution (PSD) analysis of graphite with assorted particle size: large particle (D50: 19 μm), middle sized particle (D50: 14 μm) and small particle (D50: 11 μm) (Figures S1 and S2, Table S1). DEM was utilized for estimating packing density depending on the blending ratio of different sized graphite and a ternary contour map of packing density for blendings is shown in Figure 2(a). In this simulated map, high packing density indicates high tap density of powders which can be pressed with relatively lower pressure. The highest packing density was observed in the case of 50% large particles blending with 50% small particles out of all cases, while the lowest packing density was exhibited with large size particles only. According to the previous work regarding a disordered packing theory, a maximum packing fraction is usually shown when 20%~30% of small particles are blended with large particles.[37] Besides particle size, polydispersity and shape are also known as crucial factors for the random close packing property.[38] The reason why there is some discrepancy in value between this work and others can be elucidated by considering both effects of size and polydispersity.

Based on the simulation results, we fabricated material having wide particle size distribution graphite (WD-G) and high
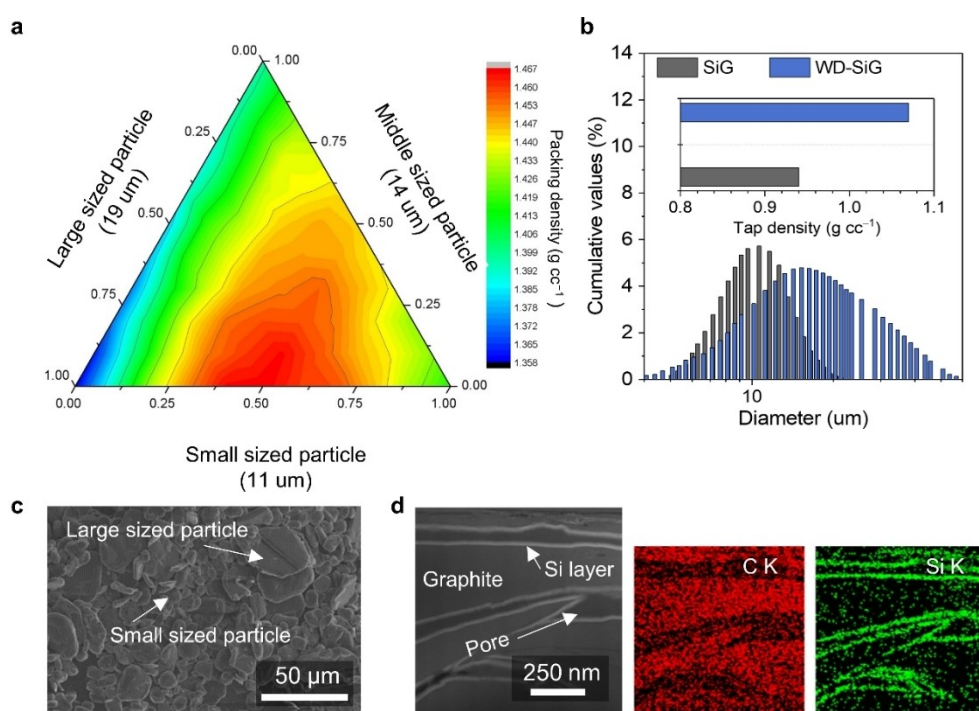

Figure 2. Materials selection, fabrication, and characterization based on the packing simulation. a) DEM simulation regarding packing density depending on mixed ratio of the different sized particles. b) Statistical analysis of SiG and WD-SiG diameter variation. c) SEM images of WD-SiG. d) TEM images of cross-sectional WD-SiG.

packing density with simple mixing of different sizes of graphite. The small particle graphite was chosen as a comparative sample of graphite (G) because it has the highest packing density among the three samples. Consequently, we synthesized both Si-coated WD-G (WD-SiG) and G (SiG) via gas decomposition of SiH_4 as in our previous study of Si/graphite composite. Particle size distribution was similar before and after Si coating because the nano thin-film Si coating might not affect the micron-sized graphite particles (Table S2). We noticed that particle distribution of WD-SiG is wider than that of SiG (Figure 2b) and the tap density of WD-SiG (1.07 g cc^{-1}) is higher than that of SiG (0.94 g cc^{-1}), which coincides with the DEM simulation results. In the scanning electron microscope (SEM) image, WD-SiG presents a wide range of particle size spanning from 4 μm to almost 50 μm, which is consistent with the PSD analysis (Figure 2c). Furthermore, through cross-sectional transmission electron microscope (TEM) images and corresponded energy-dispersive spectroscopy (EDS) mapping of carbon and Si, we observed that a thin Si-layer with the thickness of 15 nm is evenly coated on the graphite surface as shown in Figure 2(d) (high magnified TEM images and X-ray diffraction (XRD) patterns of WD-SiG are presented in Figures S3 and S4).

To further investigate the effectiveness of both WD-SiG and SiG in terms of stress evolution when computationally designed electrodes are under pressure, a calendering simulation (DEM) was conducted. In this simulation, we assumed that electrode composition only includes the active materials (WD-SiG and SiG) without any conducting materials or binders such as SBR and CMC unlike the real electrode for electrochemical analysis. The pressure was applied to each electrode until its density reached to 1.75 g cc^{-1} (Figure 3a and b). At the electrode density of 1.3 g cc^{-1}, stress is highly intensified to all particles of SiG, especially located at the pressed side. In contrast, relatively low-stress evolution happens as well as most of the particles sustain their normal state without any stress in the WD-SiG electrode. The calculated force applied to the particle in the SiG is at least three times higher than that of WD-SiG at the electrode density of 1.3 g cc^{-1} (Figure 3c). At the electrode density of 1.75 g cc^{-1}, the maximum force of WD-SiG and SiG is 1.39 and 2.21 mN, respectively (Figure 3d). Although this value gap between WD-SiG and SiG is narrowing as the electrode density increases, WD-SiG demonstrated still low-stress intensification during the calendering process, which led to securing the structure of Si anodes. However, controlling the particle size distribution might be limited to mitigate the stress evolution at the extremely high electrode density of over 1.75 g cc^{-1} and the details will be discussed in material and electrochemical characterization.

To confirm whether the stress evolution originating from the different particle size distributions of WD-SiG and SiG during calendering process affects its morphology and electrode condition, we conducted the pellet density test. Before
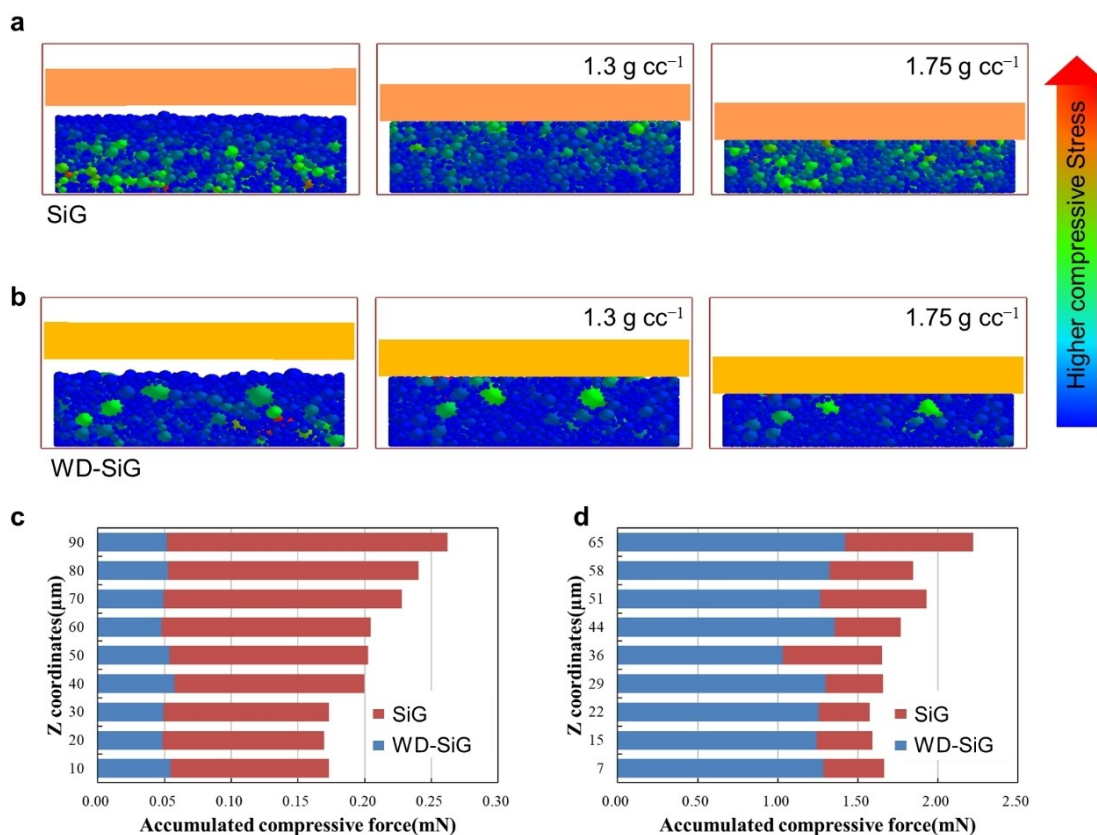

Figure 3. DEM Simulation concerning the stress evolution of particles in the electrode during calendering process. Compressive stress of each particle at electrode density of 1.75 g cc^{-1} in a) SiG and b) WD-SiG. Accumulated compressive force at different electrode density of c) 1.3 g cc^{-1} and d) 1.75 g cc^{-1}.

fabricating the pellet, both the WD-SiG and SiG were mixed with SBR, CMC, and conductive agents in a water solvent. The prepared slurry was then dried and sieved to produce fine powder for pellet. Pellets require a binder to make them have not only a good shape without cracks but also properties similar to those of electrode. The powder of the WD-SiG and SiG was placed in a cylindrical container and pressed through the pressing machine with various pressure of 3.8, 9.6, 19.2, 38.4, and 48.0 ton cm^{-2} (Figure 4a). Pellets of WD-SiG exhibited a higher density than that of SiG at the same pressure, indicating that it has high packing density and little resistance to be pressed, which corresponds with the simulation results. The springback test, in which height of the pellet (pressed with 9.6 ton cm^{-2}) was measured after 6 hours and then compared to pristine pellet, shows that the pellet height of SiG was increased more than that of WD-SiG (Figure 4b). This is because the high-stress intensification (originating from the highly pressed particles as shown in Figure 4c) applied to the SiG particles has more propensity to decrease than that of WD-SiG.

To investigate morphological changes of WD-SiG and SiG in the particle level, we fabricated the electrode with the same composition of pellet and carried out the calendering process to make its electrode density 1.6 g cc^{-1}. Cross-sectional low magnified SEM images of the SiG electrode present highly pressed particles, while those of WD-SiG show that it preserves its spherical morphology even after the calendering process (Figure 4c and f). We also observed that pressed particles lead to the crack and fracture of Si and detachment of Si-layer from the graphite surface in the high magnified SEM images obtained under back-scattered electron mode (Figure 4d and e).In contrast, there was a well attached Si-layer in the WD-SiG electrode, because the wide particle size distribution had the low-stress intensification during the calendering process (Figure 4g and h). Note that morphological change of WD-SiG does not occur and it maintains its structure at an electrode density of 1.6 g cc^{-1}, bringing about the restrained by-products formation and electrical contact loss during (de)lithiation. However, we discovered that WD-SiG does not maintain its morphological integrity and was deformed at an extremely high electrode density of 1.9 g cc^{-1} as shown in Figure S5, which coincides with the calendering simulation results.
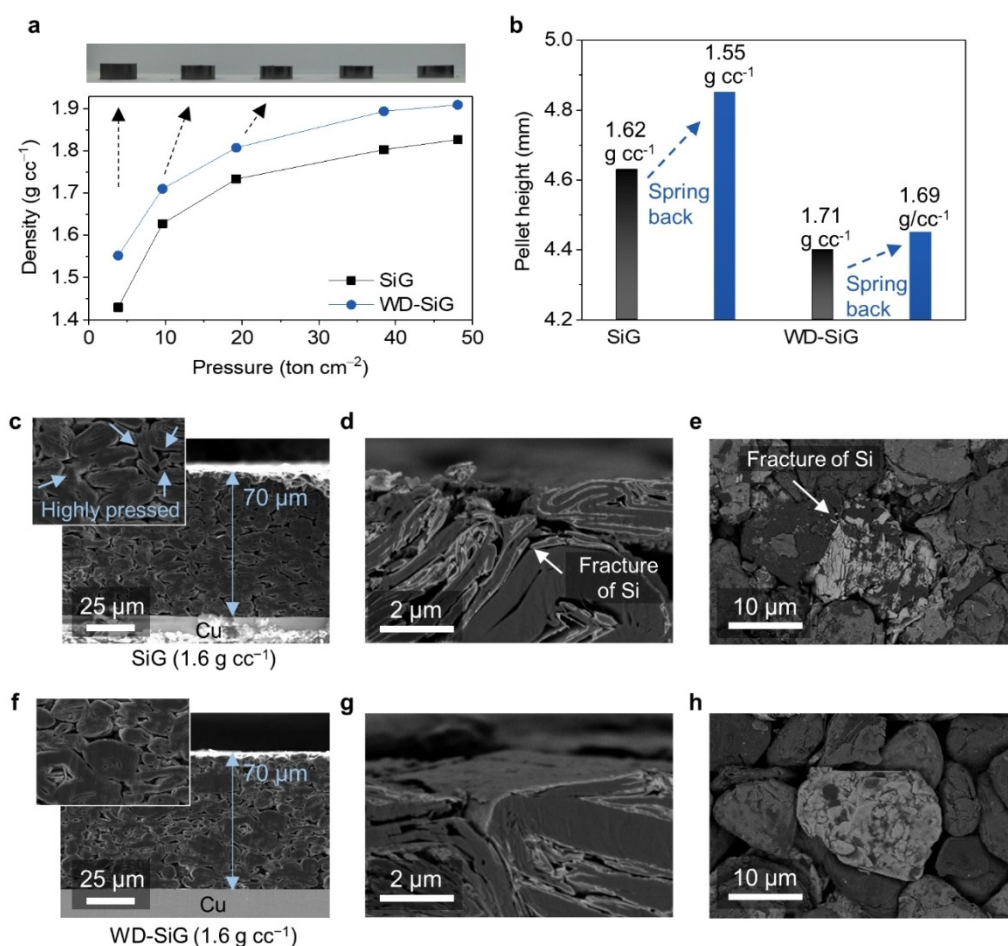

Figure 4. Mechanical stability of anodes during calendering process. a) Pellet density of SiG and WD-SiG according to the different pressure in range from 3.8 to 48.0 ton cm^{-2} and a corresponded photograph of WD-SiG pellet. b) Measurement of pellet height after pressing and its spring back. Cross-sectional SEM images of c) SiG and f) WD-SiG with an inset of magnified SEM images. Cross-sectional and top-view of d, e) SiG and g, h) WD-SiG under back-scattered electron mode enabling to clearly observe the Si with white color.

Batteries & Supercaps

Research Article
doi.org/10.1002/batt.202200136

Chemistry Europe
European Chemical
Societies Publishing

We examined the electrochemical performance of WD-SiG and SiG anodes. The initial specific capacity and CE of SiG at the electrode densities of 1.0, 1.6, and 1.8 g cc^{-1} were investigated. There are differences between the SiG without pressing (electrode density of 1.0 g cc^{-1} exhibiting the specific capacity of 507 mAh g^{-1} and CE of 95.5%) and SiG with pressing (electrode density of 1.8 g cc^{-1} showing the specific capacity of 489 mAh g^{-1} and CE of 90.4%). To find out the reasons for such differences, we investigated a differential capacity (dQ/dV) plot characterizing the (de)lithiation of each anode for the first cycle (Figure S6). The plots of SiG with electrode densities of 1.6 and 1.8 g cc^{-1} featured peaks assigned to the 0.85 V, which indicates that electrolyte decomposition (forming SEI layer) occurs (Figure 5a). Such phenomenon originates from the increased exposure of Si surface to the electrolyte owing to the pulverization and detachment of Si-layer during the calendering process, which leads to the decreased initial CE. Furthermore, reduction of initial specific capacity might be coming from some damaged Si, which is expected to cause the electrical contact loss. However, such peak assigned to the 0.85 V does not appear until an electrode density of 1.6 g cc^{-1} in case of WD-SiG (Figure 5b), implying that the wide particle size distribution strongly prevents the pulverization and detachment of Si-layer during calendering process. Nevertheless, the electrode of WD-SiG at 1.8 g cc^{-1} demonstrated a severe drop in the specific capacity and CE. To verify whether the adverse effects of specific capacity/CE drop are coming from the damaged Si or not, voltage profiles at the first cycle of pristine graphite without any Si coating were also analyzed. The intensity of peaks assigned to the 0.85 V is not changed even after pressing until an electrode density of 1.8 g cc^{-1} and capacity and CE drop does not occur in the pristine graphite electrode (Figure S7). These results imply that the shape and morphology of the Si-layer mainly influence the electrochemical properties.

Based on electrochemical performance depending on the degree of pressing, we compared WD-SiG and SiG electrodes according to the electrode density ranging from 1.0 to 1.8 g cc^{-1}. As the electrode density increases, the initial specific capacity and CE of SiG gradually decrease. However, those of WD-SiG are almost sustained until 1.6 g cc^{-1} and suddenly dropped at 1.7 and 1.8 g cc^{-1}. It reveals that WD-SiG could preserve Si-layer to some degree of electrode density (1.6 g cc^{-1}) which has been applied to industrial standard electrochemical evaluation conditions. The sudden drop in initial capacity and CE at 1.7 and 1.8 g cc^{-1} coincide with the simulation result of the dramatically increased stress evolution at that electrode density (Figure 5c).

We investigated the influence of the damaged Si-layer on the cycling performance using a half-cell configuration. The capacity retention of electrode density of 1.0 g cc^{-1} is the best among SiG anodes, implying that damaged Si-layer leads to the
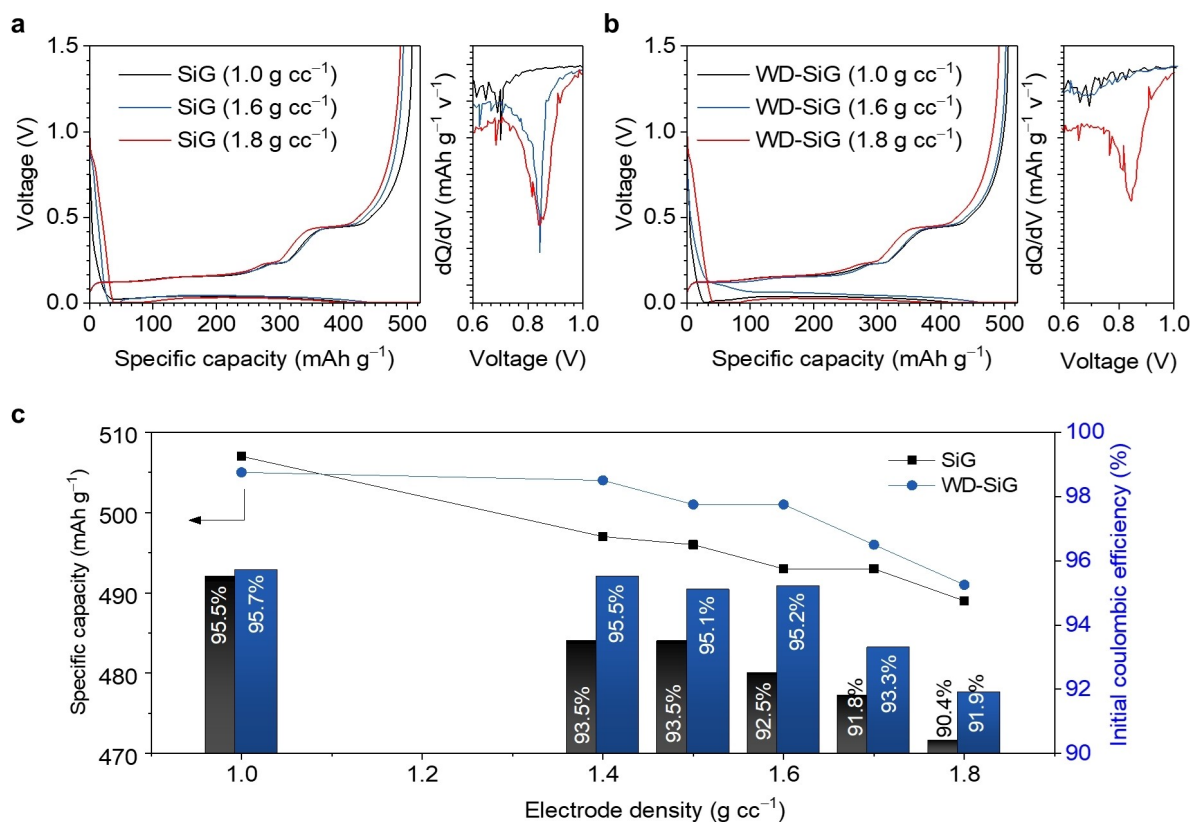

Figure 5. Electrochemical characterization of the SiG and WD-SiG anode during pre-charging and discharging process. Voltage profiles of a) SiG and b) WD-SiG at first cycle in different electrode density of 1.0, 1.6, and 1.8 g cc^{-1} and corresponded dQ/dV plots during lithiation. c) Specific discharge capacity and initial CE of SiG and WD-SiG at different electrode density in range from 1.0 to 1.8 g cc^{-1}.

Batteries & Supercaps

Research Article
doi.org/10.1002/batt.202200136

Chemistry
Europe
European Chemical
Societies Publishing

unstable SEI formation during cycles and it becomes severe as the electrode density is increased (Figure 6a). We noticed a slight increase of specific capacity in SiG electrode at 1.8 g cc^{-1} during the initial 20 cycles. Such phenomenon might be derived from the loss of electrolyte penetration to the electrode inside because the low porosity of densely packed SiG intensely blocks the pathway of electrolyte at the initial cycle. In contrast, WD-SiG anode with an electrode density of 1.6 g cc^{-1} exhibits the best performance, which is the case of SiG (Figure 6b). These results are expected to be the increased electrical contact between the particles after the calendering process without cracked Si-layer. Nevertheless, capacity retention of WD-SiG with the electrode density of 1.8 g cc^{-1} is inferior to all the others because the negative effect of pulverized Si-layer is more influenceable than the positive effect of increased electrical contact in terms of electrochemical performance.

The critical role of the WD-SiG on the electrode thickness change was revealed. We measured the SiG electrode swelling ratio in the situation of the different electrode densities ranging from 1.0 to 1.8 g cc^{-1} at the lithiated state of half-cell configuration in each cycle of 1, 10, 20, 50. The electrode swelling ratio tends to increase as the electrode density increases and cycles last (Figure 6c). In terms of electrode density, electrode swelling ratio at high electrode density with minimized empty space coming from the closely packed particles in the electrode is more likely to increase due to Si expansion during lithiation. In comparison with WD-SiG, it has a relatively lower electrode swelling ratio than that of SiG (Figure 6d). It is expected that highly pressed particles with almost non-porous structure and unstable SEI formation originating from the damaged Si-layer in SiG are increasing the electrode swelling ratio during cycles.

Commercial feasibility was explored using pouch-type full-cell comprising lithium cobalt oxide (LCO) cathode and both the WD-SiG and SiG anodes. (Details of the testing protocol and electrode information can be found in the method and Table S3, respectively, and voltage profile of LCO is shown in Figure S8.) At the electrode density of 1.6 g cc^{-1}, WD-SiG/LCO demonstrated superior capacity retention compared with SiG/LCO as shown in Figure 6(e) (full-cell formation is presented in Figure S9). To highlight the outstanding performance of WD-SiG, we compared it to previously reported carbon (or graphite) and Si-based composite anodes as shown in Table S4. We believe that WD-SiG exhibits the low-stress intensification between particles when the calendering process is carried out, leading to the preservation of free volume inside particles and
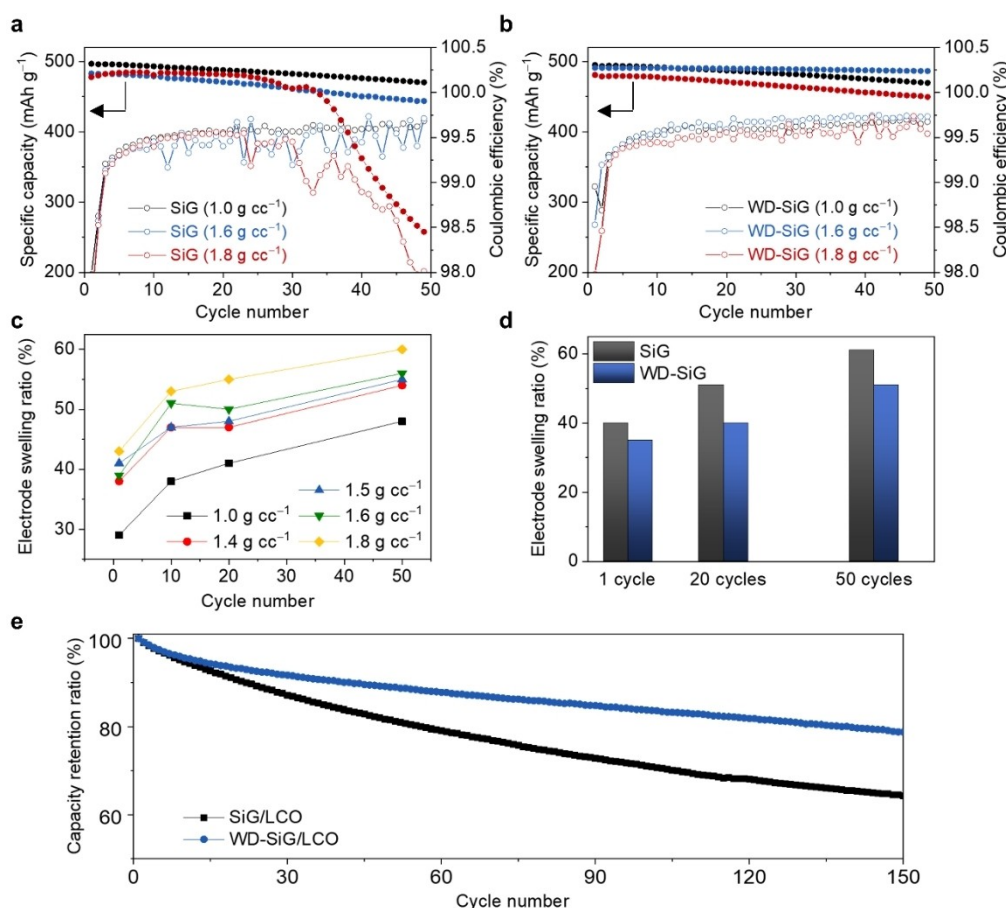

Figure 6. Electrochemical characterization of the SiG and WD-SiG anodes. Cycling performance including reversible capacity and cycling CE of half-cell regarding a) SiG and b) WD-SiG in the potential range from 0.005 to 1.0 V for 50 cycles at different electrode density of 1.0, 1.6, and 1.8 g cc^{-1}. c) The change of electrode thickness of WD-SiG at lithiated state at different electrode density in range from 1.0 to 1.8 g cc^{-1}. d) Comparison of electrode thickness change of SiG and WD-SiG. e) Discharge capacity for 150 cycles at a (dis)charge rate of 1 C in the potential range from 2.7 to 4.2 V.

Si-layer at the high electrode density. Such phenomena finally render substantial electrochemical performance such as initial specific capacity, CE, low electrode swelling ratio, and cyclability.

Conclusion

In summary, the calculation of the packing density depending on the different particle size distribution and stress evolution regarding each particle during the calendering process was conducted through the DEM simulation technique. Based on the systematic simulation, WD-SiG with a wide particle size distribution was synthesized via gas decomposition of silane gas using a mixture of commercially utilized graphite with assorted particle sizes for realizing high energy lithium-ion batteries. This anode preserving its morphological integrity and securing void space under high pressure allows it to be pressed until electrode density up to $1.6 \, g \, cc^{-1}$ while maintaining the exceptional electrochemical performance of high initial specific capacity, CE, low electrode swelling ratio, and excellent cycling stability. Conversely, SiG without controlling the particle size distribution is much more susceptible to pulverization during the calendering process, leading to the poor electrochemical properties. In conclusion, such a unique design of wide particle size distribution paves the way for alloy-typed high volume expansion anodes with the porous structure for high-energy-density and -stability lithium-ion batteries.

Supporting Information

Supporting Information is available from the Wiley Online Library or from the author.

Acknowledgements

Conflict of Interest

The authors declare no conflict of interest.

Data Availability Statement

The data that support the findings of this study are available in the supplementary material of this article.

[1] M. Armand, J.-M. Tarascon, *Nature* **2008**, *451*, 652.
[2] S. Chu, A. Majumdar, *Nature* **2012**, *488*, 294.
[3] G. Crabtree, E. Kocs, L. Trahey, *MRS Bull.* **2015**, *40*, 1067.
[4] G. Jeong, Y.-U. Kim, H. Kim, Y.-J. Kim, H.-J. Sohn, *Energy Environ. Sci.* **2011**, *4*, 1986.
[5] J. Ma, J. Sung, J. Hong, S. Chae, N. Kim, S.-H. Choi, G. Nam, Y. Son, S. Y. Kim, M. Ko, J. Cho, *Nat. Commun.* **2019**, *10*, 1–10.
[6] Y. Son, H. Cha, C. Jo, A. S. Groombridge, T. Lee, A. Boies, J. Cho, M. De Volder, *Mater. Today* **2021**, *21*, 100838.
[7] M. N. Obrovac, V. L. Chevrier, *Chem. Rev.* **2014**, *114*, 11444.
[8] S. Park, J. Sung, S. Chae, J. Hong, T. Lee, Y. Lee, H. Cha, S. Y. Kim, J. Cho, *ACS Nano* **2020**, *14*, 11548.
[9] J. Sung, N. Kim, J. Ma, J. H. Lee, S. H. Joo, T. Lee, S. Chae, M. Yoon, Y. Lee, J. Hwang, S. K. Kwak, J. Cho, *Nat. Energy* **2021**, *6*, 1164.
[10] S.-H. Choi, G. Nam, S. Chae, D. Kim, N. Kim, W. S. Kim, J. Ma, J. Sung, S. M. Han, M. Ko, H.-W. Lee, J. Cho, *Adv. Energy Mater.* **2018**, *9*, 1803121.
[11] J. Ma, J. Sung, Y. Lee, Y. Son, S. Chae, N. Kim, S. H. Choi, J. Cho, *Adv. Energy Mater.* **2020**, *10*, 1903400.
[12] Y. Son, J. Sung, Y. Son, J. Cho, *Curr. Opin. Electrochem.* **2017**, *6*, 77.
[13] S. Chae, M. Ko, K. Kim, K. Ahn, J. Cho, *Joule* **2017**, *1*, 47.
[14] Y. Jiang, D. Mu, S. Chen, B. Wu, Z. Zhao, Y. Wu, Z. Ding, F. Wu, *J. Alloys Compd.* **2018**, *744*, 7.
[15] H. Kim, M. Seo, M. H. Park, J. Cho, *Angew. Chem. Int. Ed.* **2010**, *49*, 2146.
[16] X. H. Liu, L. Zhong, S. Huang, S. X. Mao, T. Zhu, J. Y. Huang, *ACS Nano* **2012**, *6*, 1522.
[17] Y. Son, J. Ma, N. Kim, T. Lee, Y. Lee, J. Sung, S.-H. Choi, G. Nam, H. Cho, Y. Yoo, J. Cho, *Adv. Energy Mater.* **2019**, *9*, 1803480.
[18] J. Wang, H. Luo, Y. Liu, Y. He, F. Fan, Z. Zhang, S. X. Mao, C. Wang, T. Zhu, *Nano Lett.* **2016**, *16*, 5815.
[19] N. Liu, Z. Lu, J. Zhao, M. T. McDowell, H. W. Lee, W. Zhao, Y. Cui, *Nat. Nanotechnol.* **2014**, *9*, 187.
[20] S. Chae, M. Ko, S. Park, N. Kim, J. Ma, J. Cho, *Energy Environ. Sci.* **2016**, *9*, 1251.
[21] S. Jeong, X. Li, J. Zheng, P. Yan, R. Cao, H. J. Jung, C. Wang, J. Liu, J.-G. Zhang, *J. Power Sources* **2016**, *329*, 323.
[22] Y. Li, K. Yan, H.-W. Lee, Z. Lu, N. Liu, Y. Cui, *Nat. Energy* **2016**, *1*, 15029.
[23] J. Zhao, H.-W. Lee, J. Sun, K. Yan, Y. Liu, W. Liu, Z. Lu, D. Lin, G. Zhou, Y. Cui, *Proc. Natl. Acad. Sci. USA* **2016**, *201603810*.
[24] X. Li, P. Yan, X. Xiao, J. H. Woo, C. Wang, J. Liu, J.-G. Zhang, *Energy Environ. Sci.* **2017**, *10*, 1427.
[25] J. Sung, J. Ma, S. H. Choi, J. Hong, N. Kim, S. Chae, Y. Son, S. Y. Kim, J. Cho, *Adv. Mater.* **2019**, *31*, 1900970.
[26] Y. Lee, T. Lee, J. Hong, J. Sung, N. Kim, Y. Son, J. Ma, S. Y. Kim, J. Cho, *Adv. Funct. Mater.* **2020**, *30*, 2004841.
[27] S. Chae, S. H. Choi, N. Kim, J. Sung, J. Cho, *Angew. Chem. Int. Ed.* **2020**, *59*, 110.
[28] S. Chae, S. Park, K. Ahn, G. Nam, T. Lee, J. Sung, N. Kim, J. Cho, *Energy Environ. Sci.* **2020**, *13*, 1212.
[29] M. Ko, S. Chae, J. Ma, N. Kim, H.-W. Lee, Y. Cui, J. Cho, *Nat. Energy* **2016**, *1*, 16113.
[30] S. Chae, N. Kim, J. Ma, J. Cho, M. Ko, *Adv. Energy Mater.* **2017**, *7*, 1700071.
[31] Y. Jin, S. Li, A. Kushima, X. Zheng, Y. Sun, J. Xie, J. Sun, W. Xue, G. Zhou, J. Wu, *Energy Environ. Sci.* **2017**, *10*, 580–592.
[32] J. Wang, L. Liao, Y. Li, J. Zhao, F. Shi, K. Yan, A. Pei, G. Chen, G. Li, Z. Lu, Y. Cui, *Nano Lett.* **2018**, *18*, 7060.
[33] Y. Son, N. Kim, T. Lee, Y. Lee, J. Ma, S. Chae, J. Sung, H. Cha, Y. Yoo, J. Cho, *Adv. Mater.* **2020**, *32*, 2003286.
[34] D. C. Lam, M. Nakagawa, *J. Ceram. Soc. Jpn.* **1994**, *102*, 133.
[35] D. R. Dinger, J. E. Funk, *MRS Bull.* **1997**, *22*, 19.
[36] X. Ye, Y. Li, Y. Ai, Y. Nie, *Adv. Powder Technol.* **2018**, *29*, 2280.
[37] R. S. Farr, R. D. Groot, *Chem. Phys.* **2009**, *131*, 244104.
[38] D.-W. Chung, P. R. Shearing, N. P. Brandon, S. J. Harris, R. E. García, *J. Electrochem. Soc.* **2014**, *161*, A422.